Intermetallics 112 (2019) 106501

Contents lists available at ScienceDirect

Intermetallics

journal homepage: www.elsevier.com/locate/intermet

Ab initio simulations of the atomic and electronic environment around B in Fe–Nb–B metallic glasses

C.C. Yuan[a,b], C. Deng[a], H.P. Zhang[c], M.Z. Li[c,*], B.L. Shen[a,**]

[a] School of Materials Science and Engineering, Jiangsu Key Laboratory for Advanced Metallic Materials, Southeast University, Nanjing, 211189, China
[b] Department of Physics, City University of Hong Kong, 83 Tat Chee Avenue, Kowloon, Hong Kong, China
[c] Department of Physics, Beijing Key Laboratory of Opto-electronic Functional Materials and Micro-nano Devices, Renmin University of China, Beijing, 100872, China

ABSTRACT

By using *ab initio* molecular dynamical simulation, the local atomic and electronic environment around B atoms in ternary Fe–Nb–B alloys was investigated in details. We find that, with a large amount of B addition, abundant direct B–B bonds promote the propagation of prisms-like B-centered < 0 3 6 0 > polyhedron instead of antiprisms-like < 0 2 8 0 > polyhedron in Fe–Nb–B system. < 0 3 6 0 > polyhedron has a similar atomic configuration as the only B-centered < 0 5 4 0 > polyhedron in metastable $Fe_{23}B_6$ phase. It causes that the $Fe_{23}B_6$ phase rather than simple bcc α-Fe phase forms as the primary crystallization phase in Fe-rich system via the direct B–B bonding. Such a strong B–B covalent bonding as indicated by an obvious pseudogap in the density of states of *p*-orbital of B in the vicinity of Fermi level and the high charge density distribution between B–B bonds, also benefits the formation of skeleton networks by the vertex, edge and face sharing of < 0 5 4 0 > polyhedra in $Fe_{23}B_6$ phase. These complex crystallization modes and directional bonding structures introduced by the covalent effect of metalloid B are the structural origin for the excellent glass-forming ability of B-rich systems. In addition, the B alloying also enhances the average magnetic moments of Fe. However, the negative spin polarization of both Nb and B eventually causes a worse magnetism. Thus, for maintaining a high magnetic performance and formability in Fe–Nb–B system, the proper metalloid addition should be considered for material design. Our studies help us better understand the structural origin for the formation of metallic glass and offer a potential strategy for designing ferromagnetic glassy alloys with the outstanding formability as well as magnetism.

1. Introduction

As a traditional ferrous bulk glassy and nanocrystalline alloy system [1,2], Fe–Nb–B metallic glass (MG) system has drawn much attention due to its excellent performances [3,4], especially in the field of soft magnetic materials. Boron element as a metalloid-element additive in Fe–Nb–B system can effectively tailor glass formation and crystallization procedure. Some studies show the minor addition of B favors the improvement of the glass-forming ability (GFA) of Fe-based MGs, the alloys with B-rich compositions have wide supercooled liquid regions [5–7]. When the content of B is less than 10 at.% [6,7], e.g. in $Fe_{84}Nb_7B_9$ and $Fe_{80}Nb_{10}B_{10}$ systems, there is almost no supercooled liquid region shown in experiments. Similar phenomenon has also been observed in Fe–Zr–B [8], Fe–Zr–B–Nb [9], and other Fe-based multicomponent glassy alloys. Crystallization mode also closely correlates with B content [6,7,10,11]. The amorphous phase in Fe–Nb–B system with less B prefers to form a primary phase of α-Mn type and then directly transforms into a stable single phase (α-Fe type) during annealing. While a complex metastable phase that $Fe_{23}B_6$-type structure, is formed as a primary crystallization phase in B-rich Fe–Nb–B system, corresponding to a good GFA. However, the excellent GFA with metalloid element alloying always accompanies with the sacrifice of soft magnetic performance of Fe-based glassy alloy system [1], which severely degrades its commercial value in magnetic applications. Previous studies show that metalloid B elements can influence the magnetism of glassy alloys by transferring electron from transition metal elements to themselves [12,13]. Besides of the charge transfer effect [12,13], bonding hybridization effects [14], and short-range ordered structure [15] are proposed to be related with the magnetism of transition metal-based glassy alloys. Nevertheless, due to the limit of both experiments and theories, the relationship between local structure and GFA/magnetism has not been established.

Recently, Reverse Monte Carlo simulation [16–22] combined with the experimental data obtained from synchrotron X-ray diffraction [16–18], extended X-ray absorption fine structure [18–20], neutron diffraction [21] or reduced density functions derived from electron diffraction [22] is conducted as a popular method for constructing three-dimensional atomic configuration of metallic glass, in favor of detecting local atomic structure. A great effort on atomic structure based on Reverse Monte Carlo simulation has also been made to explain the different GFA and magnetic properties of Fe–Nb–B system [6,11,23]. However, due to the small contribution of boron-related

* Corresponding author.
** Corresponding author.
E-mail addresses: maozhili@ruc.edu.cn (M.Z. Li), blshen@seu.edu.cn (B.L. Shen).

https://doi.org/10.1016/j.intermet.2019.106501
Received 11 October 2018; Accepted 5 May 2019

atomic pairs to the experimental diffraction patterns [23], the atomic configuration around B is still not clear. *Ab initio* molecular dynamical simulation, which does not require the data from experiment and has an advantage in high accuracy, is a convince tool in studying the local atomic structure of glassy alloys and their melts [20,24,25]. Numerous studies based on *ab initio* and classical molecular dynamical simulations show that the local atomic structure around metalloid atoms is often prism-like polyhedra, which is quite different from the icosahedron-like atomic configuration around metal atom as found in metal-metal-based glasses [26–30]. Understanding of local atomic environment around B atoms is important for us to seek structural origin of glass formation in metalloid-metal-based systems. In addition, a detailed electronic structural information from *ab initio* simulation can help us further understand the magnetic properties of Fe-based alloy [24].

In this paper, we use *ab initio* molecular dynamical simulation method to study the evolution of local atomic configuration around metalloid B element of $Fe_{80}Nb_{10}B_{10}$, $Fe_{70}Nb_{10}B_{20}$, and $Fe_{60}Nb_{10}B_{30}$ melts and glassy alloys during cooling process. The atomic scale structural information can be obtained by partial pair correlation functions, Voronoi polyhedra and coordination number (CN). Electronic density of states (DOS) and the charge density distribution are further studied for finding the origin of the various local atomic environments. Magnetic moments of Fe, Nb, and B are calculated as well, to understand the magnetic performance of Fe–Nb–B system. In this work, by addressing the atomic and electronic configuration around B atoms, we intend to further understand the structural origin for the formation of metallic glass and find a potential way to improve both GFA and magnetic performance of ferromagnetic glassy alloys.

2. Methods

Ab initio molecular dynamical simulations for $Fe_{80}Nb_{10}B_{10}$, $Fe_{70}Nb_{10}B_{20}$, and $Fe_{60}Nb_{10}B_{30}$ MG system were performed using the projector augmented-wave method within the density functional theory as implemented in the Vienna *ab initio* simulation package [31]. The generalized gradient approximation was adopted to describe the exchange-correlation function. A typical time step of 3 fs was used with the Verlet algorithm to integrate Newton's equations of motion. Only Γ point was used to sample the Brillouin zone of the supercell. The used cubic box contains 200 atoms with periodic boundary conditions applied in three directions. In order to control the temperature, the simulations were performed in the NVT (constant number, volume, temperature) ensemble with a Nosé thermostat. The systems were melted and equilibrated at 1700 K for 3000 steps to remove the memory from the initial configurations, then cooled down to 300K at a constant cooling rate of 0.2 K per step. The atomic configurations at 1700, 1500, 1300, 1100, 900, 800, 700, 600, 500, 400, and 300 K during cooling process were kept for further isothermal annealing. At these temperatures, the equilibrium volume was established by approximately keeping the internal pressure to zero within about ± 1.0 kBar and equilibrated for 2000 steps. The last 1000 configurations at each temperature were collected for structural analysis. The electronic DOS and the charge density distribution between atomic bonds were calculated with spin polarization considered.

3. Results and discussion

3.1. Pair correlation function g(r)

Fig. 1 presents the evolution of the generalized pair correlation functions of $Fe_{80}Nb_{10}B_{10}$, $Fe_{70}Nb_{10}B_{20}$, and $Fe_{60}Nb_{10}B_{30}$ melts during cooling processes. As shown by the definition of pair correlation function, $g(r)$ represents the probability of finding atoms as a function of distance r from an average center atom. The pair correlation functions of three alloys exhibit a typical liquid behavior at temperatures above 1300 K. $Fe_{70}Nb_{10}B_{20}$ and $Fe_{60}Nb_{10}B_{30}$ alloys exhibit a little change in

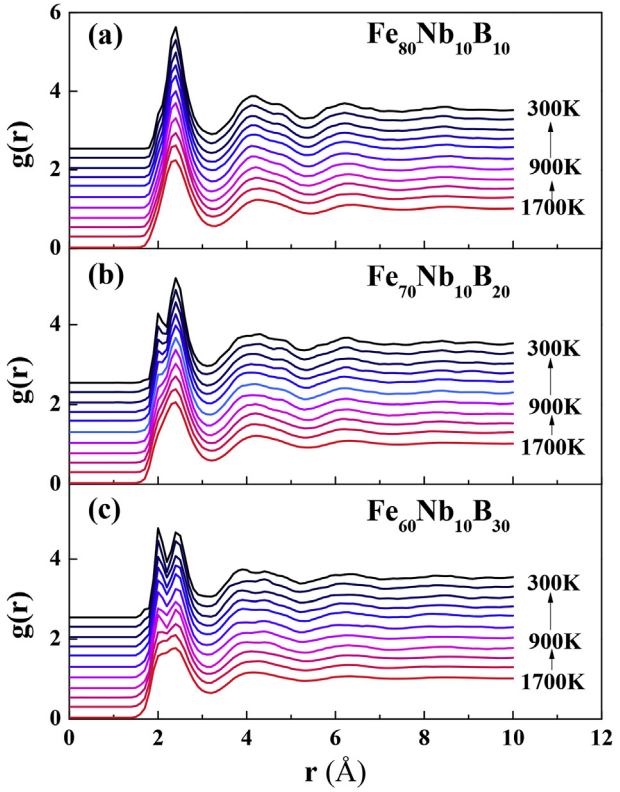

Fig. 1. Simulated temperature-dependent pair correlation function $g(r)$ of $Fe_{80}Nb_{10}B_{10}$ (a), $Fe_{70}Nb_{10}B_{20}$ (b), and $Fe_{60}Nb_{10}B_{30}$ (c) alloys.

first peak at the temperature much higher than 1300 K. With decreasing temperature, a shoulder peak on the left of the main peak emerges in both $Fe_{70}Nb_{10}B_{20}$ and $Fe_{60}Nb_{10}B_{30}$ melts. The intensity of the shoulder peaks increases with decreasing temperature. We plot the partial pair correlation functions together with generalized pair correlation functions of these three alloys at 300 K in Fig. 2. It can be found that the position of the shoulder peak corresponds to the contribution of the $g_{Fe\text{-}B}(r)$. The high concentration of Fe–B pairs in B-rich alloys causes the obvious shoulder in the main peak. The predictable splitting of the second peak in generalized $g(r)$s of Fig. 1 is originated from the large discrepancy in the correlation length of different atomic pairs at 4–6 Å, which benefits the propagation of a disordered structure.

The $g_{Fe\text{-}Fe}(r)$, $g_{Fe\text{-}Nb}(r)$, $g_{Fe\text{-}B}(r)$, $g_{Nb\text{-}Nb}(r)$, and $g_{Nb\text{-}B}(r)$ (Fig. 2(a–c)) all have a pronounced first peak and a minor second peak. Different from other partial pair correlation functions, the $g_{B\text{-}B}(r)$ has a much more remarkable second peak than the first one. In $Fe_{80}Nb_{10}B_{10}$, the first peak of $g_{B\text{-}B}(r)$ is suppressed and shifts to larger r (Fig. 2(a)). With increasing B content, the first peak of $g_{B\text{-}B}(r)$ becomes notable and sharp again, e.g. in B-rich systems such as $Fe_{70}Nb_{10}B_{20}$ and $Fe_{60}Nb_{10}B_{30}$. These composition dependent features are only found in B–B partial pair correlation functions. Thus, we further track the evolution of $g_{B\text{-}B}(r)$ upon temperature, seen in Fig. 3.

We find that, at high temperatures, the second peak of $g_{B\text{-}B}(r)$ is much more pronounced than the first peak in all of these three alloys, which indicates that B atoms do not tend to be surrounded by other B atoms in the nearest-neighbor shell and prefer to be as a second neighbor of themselves. When the temperature decreases, the intensity for the first peak of $g_{B\text{-}B}(r)$ in both of $Fe_{70}Nb_{10}B_{20}$ and $Fe_{60}Nb_{10}B_{30}$ gradually increases, while $Fe_{80}Nb_{10}B_{10}$ shows a contrary tendency. The first peak of $g_{B\text{-}B}(r)$ in $Fe_{80}Nb_{10}B_{10}$ shifts to larger r and becomes weaker with decreasing temperature, which suggests that direct B–B bonds are broken in $Fe_{80}Nb_{10}B_{10}$ system. Moreover, the different evolution tendency of the $g_{B\text{-}B}(r)$s during rapid cooling process reveals that the addition of B in Fe–Nb–B systems results in the change of local atomic

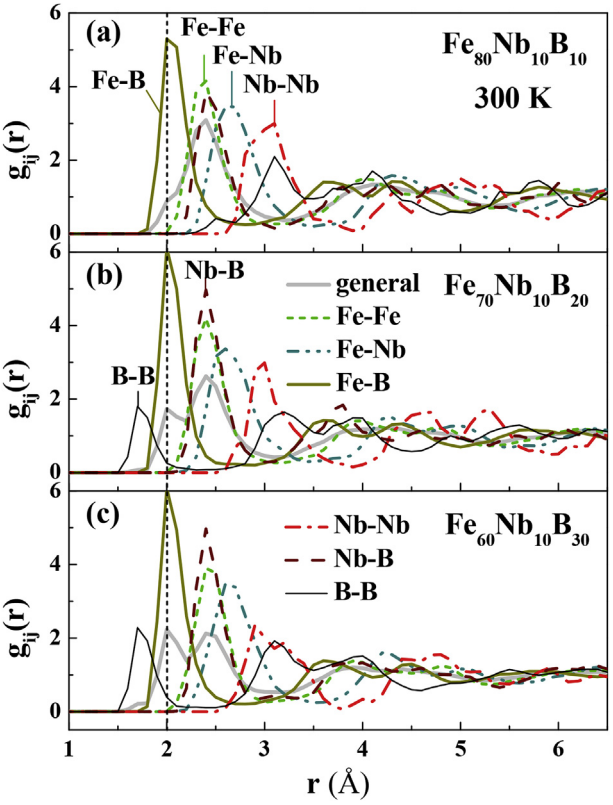

Fig. 2. Generalized and partial pair correlation functions of $Fe_{80}Nb_{10}B_{10}$ (a), $Fe_{70}Nb_{10}B_{20}$ (b), and $Fe_{60}Nb_{10}B_{30}$ (c) at 300 K (glassy state).

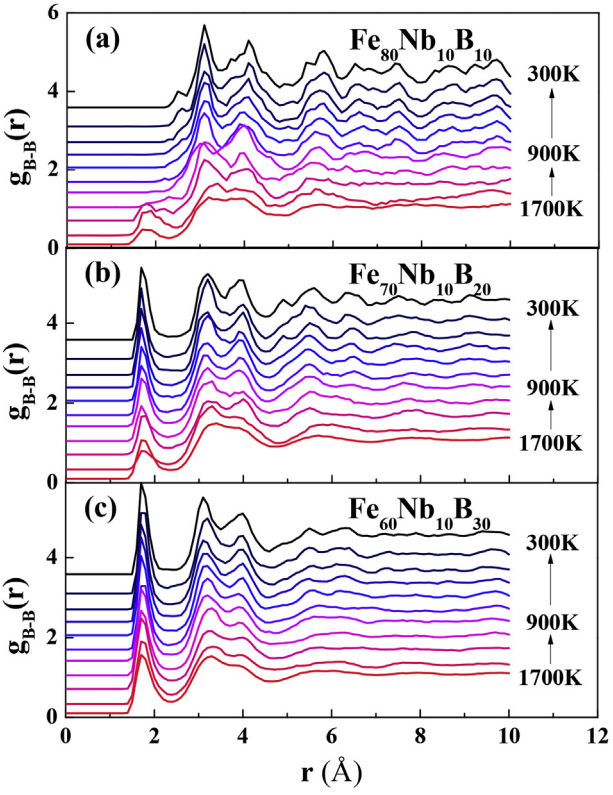

Fig. 3. Temperature-dependent B–B partial pair correlation functions of $Fe_{80}Nb_{10}B_{10}$ (a), $Fe_{70}Nb_{10}B_{20}$ (b), and $Fe_{60}Nb_{10}B_{30}$ (c).

environment around B.

3.2. Voronoi polyhedra

In order to find out such change of local atomic structure in details, Voronoi polyhedral analysis was conducted. Voronoi polyhedral analysis [32] is a sophisticated and commonly used approach to describe the local atomic structure of liquid and amorphous solids. By this approach, the perpendicular bisectors unweighted by the atomic size between the central atom and the neighboring atoms forms a Voronoi cell. Voronoi polyhedra can be indexed as $< n_3, n_4, n_5, n_6, \ldots, n_i >$, where n_i is the number of i-edge faces on the polyhedron. The total number of faces of a Voronoi polyhedron is equivalent to the coordination number (Σn_i = CN) for a given center atom [32]. Here, the neighboring atoms were identified within a cut-off distance 3.2 Å, the first minima in generalized pair correlation functions.

Fig. 4 shows the population of the 10 most dominated Voronoi polyhedra in three alloys at the temperature of 1700 and 300 K, respectively. < 0 0 12 0 > polyhedron is defined as icosahedral cluster. < 0 3 6 3 >, < 0 2 8 2 >, and < 0 1 10 2 > polyhedra are defined as icosahedral-like clusters. < 0 3 6 4 >, < 0 2 8 4 >, and < 0 3 6 5 > polyhedra are defined as distorted bcc-like clusters [21,33,34]. It can be found in Fig. 4 that Fe-centered distorted bcc-like clusters such as < 0 3 6 4 > have the largest population in three alloy melts at 1700 K. However, at amorphous state, the number of icosahedral-like clusters such as < 0 1 10 2 > cluster ultimately surpasses that of distorted bcc-like clusters such as < 0 3 6 4 >. This leads to the competition of the bcc-like clusters and icosahedral-like clusters during cooling process. When the number of icosahedral-like clusters becomes dominant in local configurations, the amorphous structure starts to form.

The excellent GFA of metal-metal-based glasses can be attributed to the icosahedron-like local structures that lead to a dense atomic packing along with lack of the translation symmetry for long-range growth of crystals [20]. For metal-metalloid-based glasses, the mechanism for glass formation is much more complex. The local atomic structure around metalloid atoms is often prism-like polyhedra that quite differ from the atomic configuration around metal atoms [30]. Since such prism-like polyhedra play a key role in determining GFA, five dominated B-centered polyhedra in Fe–Nb–B alloy systems are plotted in Fig. 5. It can be seen that < 0 2 8 0 >, < 0 2 8 1 >, < 0 3 6 0 >, and < 0 3 6 1 > polyhedra are dominant B-centered polyhedra in Fe–Nb–B alloys both at liquid (1700 K) and glassy (300 K) state. < 0 3 6 0 > polyhedron is a type of tricapped trigonal prisms (see Fig. 10 (a)) and < 0 2 8 0 > polyhedron is a type of bicapped square antiprisms (see Fig. 10 (a)) [30]. < 0 2 8 1 > polyhedron can be regarded as the distorted < 0 2 8 0 > polyhedron. Similarly, < 0 3 6 1 > polyhedron can be regarded as the distorted < 0 3 6 0 > polyhedron. < 0 2 8 0 > polyhedron is more likely to dominate in $Fe_{80}Nb_{10}B_{10}$ alloys with less B content, while < 0 3 6 0 > polyhedron is likely to dominate in B-rich $Fe_{70}Nb_{10}B_{20}$ and $Fe_{60}Nb_{10}B_{30}$ alloys. The fraction of < 0 2 8 0 > polyhedron centered by B atoms in $Fe_{80}Nb_{10}B_{10}$ alloys increases remarkably from 1700 to 300 K. While, in $Fe_{70}Nb_{10}B_{20}$ and $Fe_{60}Nb_{10}B_{30}$ alloys, the increase tendency of < 0 3 6 0 > polyhedron is much more pronounced, which becomes dominant at glassy state. The evolution of the number of < 0 3 6 0 > and < 0 2 8 0 > polyhedra during simulated cooling process is plotted in Fig. 6. In $Fe_{80}Nb_{10}B_{10}$ system, during rapid cooling process, the fraction of < 0 2 8 0 > polyhedron has a steep rising up from 8.37% to 24.8%, while < 0 3 6 0 > polyhedron only slightly increases from 6.42% to 10.35%. While in $Fe_{70}Nb_{10}B_{20}$ system, the fraction of < 0 3 6 0 > polyhedron increases quickly when the fraction of < 0 2 8 0 > polyhedron remains constant. The different change tendencies of two kinds of polyhedra during cooling process agree well with the evolution of the $g_{B\text{-}B}(r)$ with the temperature. B-centered < 0 3 6 0 > polyhedron often has another B atom in its first shell, which corresponds to the first peak that appears in the distance of

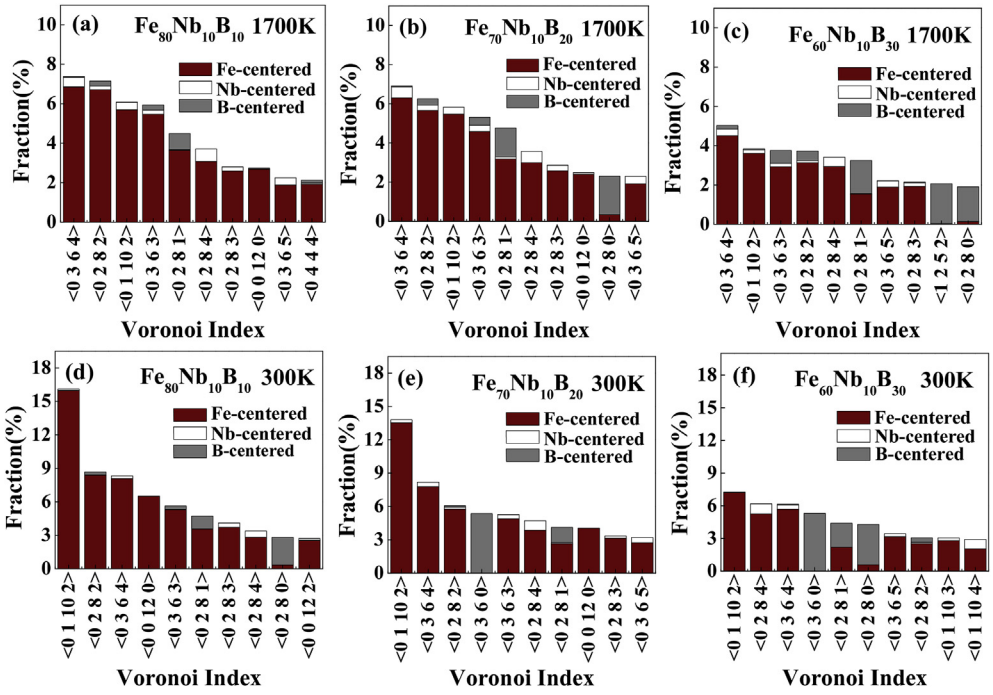

Fig. 4. Population of the 10 most dominated Voronoi polyhedra in $Fe_{80}Nb_{10}B_{10}$ (a), $Fe_{70}Nb_{10}B_{20}$ (b), and $Fe_{60}Nb_{10}B_{30}$ (c) at 1700 K (liquid state) and in $Fe_{80}Nb_{10}B_{10}$ (e), $Fe_{70}Nb_{10}B_{20}$ (f), and $Fe_{60}Nb_{10}B_{30}$ (g) at 300 K (glassy state).The filled parts of each bar indicate the percentage of Fe-centered, Nb-centered, and B-centered polyhedra of each Voronoi index, respectively.

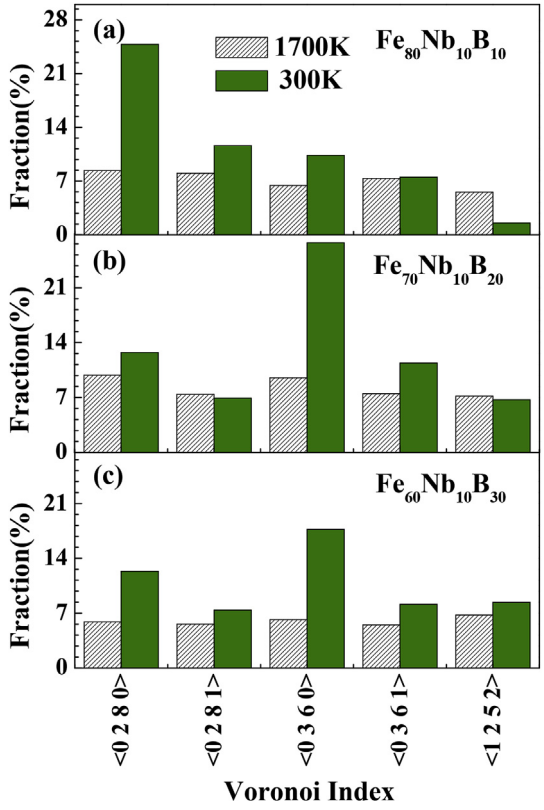

Fig. 5. Population of the 5 dominated B-centered polyhedra in $Fe_{80}Nb_{10}B_{10}$ (a), $Fe_{70}Nb_{10}B_{20}$ (b), and $Fe_{60}Nb_{10}B_{30}$ (c) at 1700 and 300 K. The fractions are normalized by the atomic number of B.

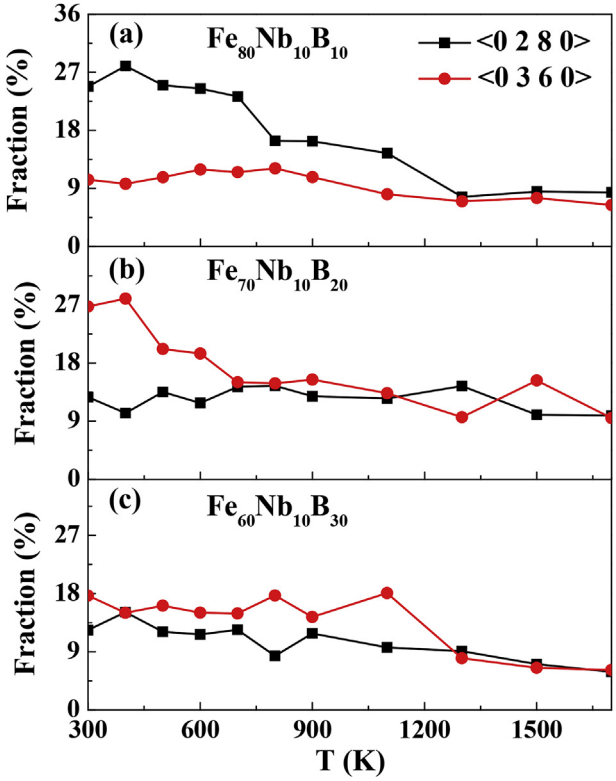

Fig. 6. The temperature dependence of < 0 3 6 0 > and < 0 2 8 0 > polyhedra during simulated cooling process, for $Fe_{80}Nb_{10}B_{10}$ (a), $Fe_{70}Nb_{10}B_{20}$ (b), and $Fe_{60}Nb_{10}B_{30}$ (c). The fractions are normalized by the atomic number of B.

1.78 Å in the $g_{B\text{-}B}(r)$. The disappearance of the first peak in $g_{B\text{-}B}(r)$ of $Fe_{80}Nb_{10}B_{10}$ at glassy state is due to the low fraction of < 0 3 6 0 > polyhedron. Therefore, a conclusion can be drawn here that in the Fe–Nb–B alloy system, B-centered prism-like < 0 3 6 0 > polyhedron is more likely to propagate with increasing B–B bonds when < 0 2 8 0 > polyhedron dominates in the alloys with low B concentration.

As shown in Fig. 6, it is obvious that the population of < 0 3 6 0 > and < 0 2 8 0 > polyhedra in $Fe_{60}Nb_{10}B_{30}$ do not change too much when the alloy system is cooled from liquid to amorphous state. To answer this question, the types of polyhedra found in three alloys are counted in Table 1. It can be found that the number of polyhedral type decreases during cooling process and the alloys containing more B atoms possesses more types of polyhedra. It indicates that the

Table 1
The number of polyhedral types centered by Fe, Nb and B atoms in Fe–Nb–B alloys at 1700K and 300K.

Alloys	Temperature (K)	Fe	Nb	B	Total
$Fe_{80}Nb_{10}B_{10}$	1700	579	386	311	693
	300	178	94	57	218
$Fe_{70}Nb_{10}B_{20}$	1700	558	419	375	711
	300	168	134	68	244
$Fe_{60}Nb_{10}B_{30}$	1700	727	580	494	948
	300	228	146	138	347

introduction of B atoms in Fe-based glassy alloy would lead to a more inhomogeneous and complex local configuration as found in their melts and glasses. During cooling process, different kinds of polyhedra will compete with each other, which causes the disappearance of certain kinds of polyhedra. This competition can explain the stable population of dominant polyhedra in B-rich $Fe_{60}Nb_{10}B_{30}$ system, independence of temperature. On the other hand, a large number of polyhedral types in alloys can prevent the formation of an ordered structure, which also benefits metallic glass formation.

3.3. Coordination number, CN and atomic bonding preferences

To further present short-range ordered structure, we also calculate the partial coordination numbers N_{ij}, average number of neighbors of a given atomic species N_i, and total coordination numbers N for three alloy systems at 1700 and 300 K, respectively, see Table 2 for details. The coordination number does not change too much from liquid to glassy state in each alloy. We also find that these three kinds of atoms have different local environments. B atoms are in the center of the small clusters (CN ≈ 11), Nb atoms are surrounded by the large clusters (CN ≈ 14–15), and Fe atoms are surrounded by the medium-sized clusters (CN ≈ 13). The atomic bonding preferences in three MGs are also calculated based on the coordination condition, seen in Fig. 7(a–c). It can be found that the chemical compositions surrounding Fe atoms are almost the same as the nominal alloy composition in each MG. While, Fe concentration surrounding both Nb and B atoms is higher than the normal composition of Fe in all three alloys, which indicates Fe atoms can be regarded as solvent atoms, where the Nb and B atoms as solute atoms are surrounded by a large amount of Fe atoms, and avoid connecting with the atoms of their same kind. This can be further confirmed by the fact that the atomic environment surrounding Nb atoms intends to comprise of more Fe and less Nb as compared with the nominal composition. A similar tendency is also shown for the compositions around B atoms. The most interesting feature in Fig. 7 is that

Table 2
Partial coordination numbers N_{ij}, average number of neighbors of a given atomic species N_i, and total coordination numbers N for $Fe_{80}Nb_{10}B_{10}$, $Fe_{70}Nb_{10}B_{20}$, and $Fe_{60}Nb_{10}B_{30}$ at 1700 and 300 K.

N_{ij} Pairs,ij	$Fe_{80}Nb_{10}B_{10}$		$Fe_{70}Nb_{10}B_{20}$		$Fe_{60}Nb_{10}B_{30}$	
	1700 K	300 K	1700 K	300 K	1700 K	300 K
Fe–Fe	10.10	10.08	9.05	9.20	7.95	8.14
Fe–Nb	1.53	1.59	1.46	1.51	1.61	1.64
Fe–B	1.17	1.14	2.33	2.18	3.69	3.61
Nb–Fe	12.26	12.74	10.21	10.56	9.68	9.85
Nb–Nb	1.00	1.15	0.97	0.80	0.74	0.70
Nb–B	1.12	1.12	2.82	2.75	4.29	4.24
B–Fe	9.33	9.15	8.14	7.63	7.38	7.23
B–Nb	1.12	1.12	1.41	1.37	1.43	1.41
B–B	0.43	0.32	1.05	0.77	2.13	1.67
N_{Fe}	12.80	12.81	12.83	12.89	13.25	13.40
N_{Nb}	14.38	15.00	14.00	14.11	14.71	14.79
N_B	10.88	10.59	10.60	9.77	10.94	10.32
N	12.76	12.81	12.50	12.39	12.70	12.61

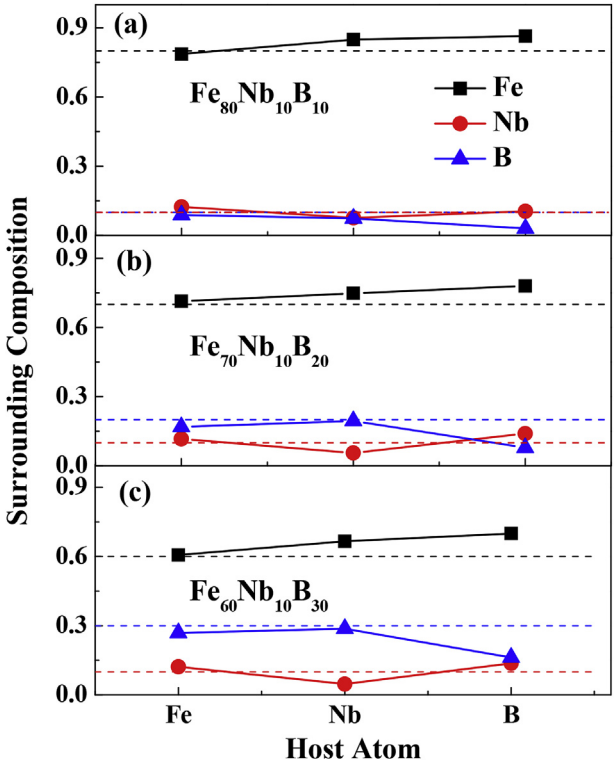

Fig. 7. Atomic bonding preference in $Fe_{80}Nb_{10}B_{10}$ (a), $Fe_{70}Nb_{10}B_{20}$ (b), and $Fe_{60}Nb_{10}B_{30}$ (c) MGs.

the B concentration around Nb and Fe atoms is almost the same as the nominal composition even in $Fe_{80}Nb_{10}B_{10}$ MGs with less B atoms as compared with that of other two alloys. The concentration of Nb that surrounds B atoms in three alloys is 10.5, 14.0, and 13.7 at.%, respectively. The nominal concentration of Nb in three alloys is 10 at.%. It implies that, besides Fe atoms, B atoms also prefer to contact with Nb. This is consistent with the result reported in the FINEMET type $Fe_{73.5}Si_{13.5}B_9Nb_3Cu_1$ amorphous alloy [35].

3.4. Electronic configuration

The spin polarized total and partial electronic DOS of $Fe_{80}Nb_{10}B_{10}$, $Fe_{70}Nb_{10}B_{20}$, and $Fe_{60}Nb_{10}B_{30}$ MGs are displayed in Fig. 8. These three DOS curves do not vary much. They all exhibit the features of electric conductor and ferromagnetism (i.e. the DOS in Fermi level is not zero and the DOS of spin up is not equal with that of spin down). The Fermi level is located right above the majority spin band and exactly on the local minimum of the minority spin band. The DOS of Fe–Nb–B, accordingly, can be divided into three bands: $-10eV < E\text{-}E_f < -6eV$ (marked as **A**), $-6eV < E\text{-}E_f < 0eV$ (marked as **B**), $0eV < E\text{-}E_f < 3eV$ (marked as **C**). **A** band is mainly constructed by B-2*s* orbital. **B** and **C** bands are contributed by B-2*p* orbital, Fe-3*d* orbital and Nb-4*d* orbital. There is an obvious pseudogap between **B** and **C** bands, indicating covalent character in electronic structure. The covalence arising from the *s-p* hybridization of B–B bonds as well as the *p-d* hybridization of B *p*-orbital and Fe/Nb *d*-orbital can be well explained according to the overlapping of Fe-3*d*, Nb-4*d*, and B-2*s* states, where *s*-DOS of B is scattered far away from the Fermi level [36]. This is the reason for the preference of B atoms surrounded by Nb and Fe atoms as the nearest neighbors shown in atomic bonding preference analysis. The results of the electronic DOS of three systems are almost the same, besides the fact that a weaker *p*-DOS of B atoms in B-rich system is observed. The weaker *p*-DOS of B observed in B-rich system is also attributed to the strong *p-d* covalent hybridization of B and other atoms.

In order to get more visual information on bonding character as well

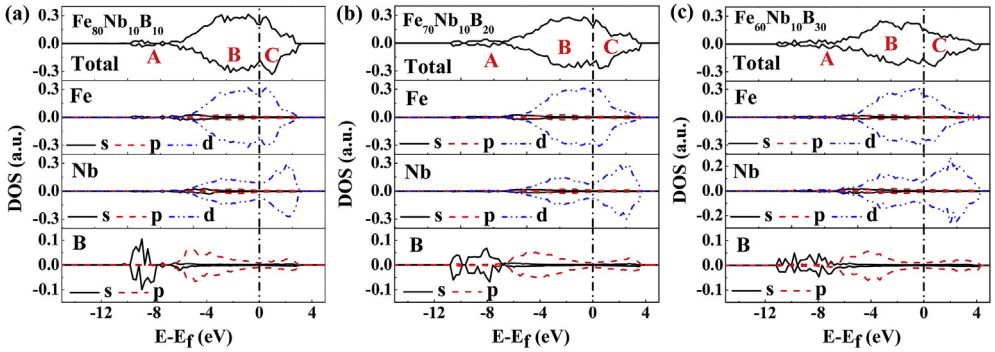

Fig. 8. Spin polarized total and partial DOS of $Fe_{80}Nb_{10}B_{10}$ (a), $Fe_{70}Nb_{10}B_{20}$ (b), and $Fe_{60}Nb_{10}B_{30}$ (c) MGs. (A, B and C are marked as the different bands for the discussion in the main text.)

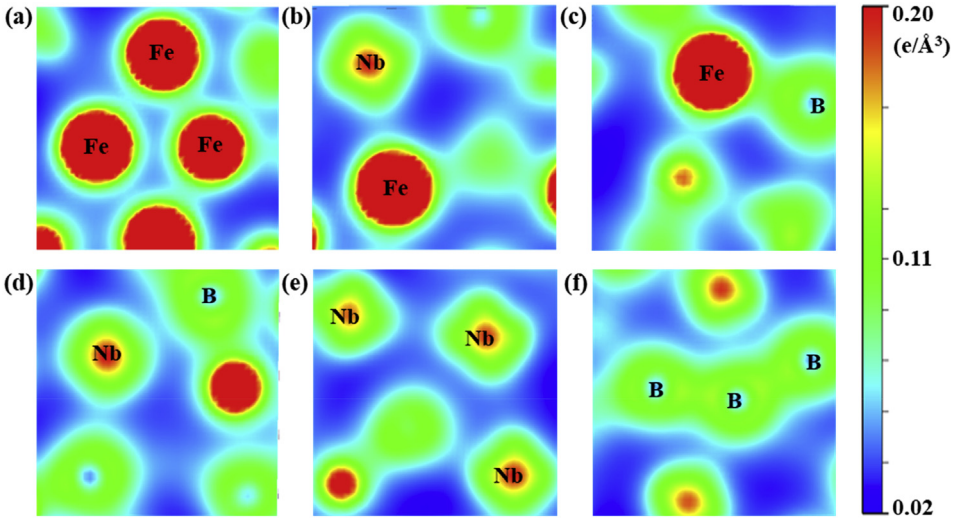

Fig. 9. Charge density distribution between Fe–Fe (a), Fe–Nb (b), Fe–B (c), Nb–Nb (d), Nb–B (e), and B–B (f) atomic pairs in $Fe_{60}Nb_{10}B_{30}$ MG.

as hybridization information between Fe, Nb, and B, the charge density distribution in $Fe_{60}Nb_{10}B_{30}$ was calculated. The information of the corresponding Fe–Fe, Fe–Nb, Fe–B, Nb–B, Nb–Nb, and B–B bonding were extracted. Fig. 9 shows a selected slice of the charge density distribution. It is seen that the metallic bonds form between Fe and Nb atoms, which can be easily identified according to the uniform distribution of charge density around Fe, Nb and their nearest neighbors. However, the charge density distributed between Fe/Nb and B is more directional, which gives rise to a kind of covalent bond between B atoms with other atoms. Here, the covalence of Fe–B and Nb–B bonds, as shown in Fig. 9 (c) and (d), can well explain the preference of B is surrounded by both Fe and Nb. Besides, we also find that the bonding strength as indicated by charge density distribution between the atomic bonds, is much stronger for B-dominated covalent bonds than metallic bonds formed between Fe–Fe, Fe–Nb, Nb–Nb atomic pairs.

3.5. Magnetic performance of Fe–Nb–B system

According to the spin polarized total and partial DOS, we can obtain magnetic performances of Fe–Nb–B system as well. It can be seen in Fig. 8 that the Fe-4*d* band splits into two main peaks, which is quite similar to the performance of bcc Fe [37]. Such two-peak structure has also been found in $Fe_{80}B_{20}$ [38], $Fe_{70}Zr_{10}B_{20}$ [39], and $Fe_{80}P_{11}C_9$ [24] glassy alloy systems by using spin-resolved photoemission or first principles simulation. Similar to the report by other Fe-based systems [24,39], the Fermi level of the Fe–Nb–B system falls right in the gap of the minority band [24]. As reported by Malozemoff et al. [40], the strong ferromagnetism occurs when the Fermi level falls in the gap of spin-down bands. Normally, the deeper is the gap, the stronger is the magnetism. It indicates that our simulated Fe–Nb–B amorphous alloy is also a strong ferromagnetism, and the magnetism is weakened upon B addition. It is consistent with the previous experimental results that the addition of metalloid alloy element leads to a poor magnetic performance of ferromagnetic system [3].

Partial magnetic moments of Fe, Nb, and B are further calculated accordingly, listed in Table 3. For Fe and Nb atoms, besides the main contribution from *d* states with an average magnetic moment, the *s* and *p* states also provide a small negative contribution to the whole magnetic moments of Fe and Nb atoms. However, the polarization of B atoms mostly comes from *p* states, which results from the *p-d* orbital hybridization of B with both Fe and Nb atoms. Consistent with the finding in the picture of partial DOS, the magnetization is dominated by Fe-3*d* states, followed by a small contribution form Nb-4*d* state and 2*p* states of B. The average magnetic moments of Fe is 0.614, 0.640, and 0.681 μ_B in $Fe_{80}Nb_{10}B_{10}$, $Fe_{70}Nb_{10}B_{20}$, and $Fe_{60}Nb_{10}B_{30}$, respectively. As shown in Table 3, B has a small magnetic moment of −0.0350, −0.0312, and −0.0109 μ_B in $Fe_{80}Nb_{10}B_{10}$, $Fe_{70}Nb_{10}B_{20}$, and $Fe_{60}Nb_{10}B_{30}$, respectively, while Nb has an average magnetic moment of −0.164, −0.145, and −0.109 μ_B in $Fe_{80}Nb_{10}B_{10}$, $Fe_{70}Nb_{10}B_{20}$, and $Fe_{60}Nb_{10}B_{30}$, respectively. It is quite smaller than the reported magnetic moment of B of about −0.1 μ_B in $Fe_{100-x}B_x$ amorphous alloy [41]. Therefore, compared to Nb, less negative spin polarization of B has a negligible effect on the reduction of total magnetization. The negative spin polarization of both Nb and B leads to a worse magnetic performance of B-rich $Fe_{60}Nb_{10}B_{30}$ as compared with other two systems, even though the average magnetic moment of Fe is the largest among others.

Table 3
Average magnetic moment of *s*, *p*, and *d* states of Fe, P, and C atoms in $Fe_{80}Nb_{10}B_{10}$, $Fe_{70}Nb_{10}B_{20}$ and $Fe_{60}Nb_{10}B_{30}$ amorphous alloys.

Composition	Magnetic moment	*s* (μ_B)	*p* (μ_B)	*d* (μ_B)	Total (μ_B)	$Total_{all}$ (μ_B)
$Fe_{80}Nb_{10}B_{10}$	Fe	−0.0021	−0.0112	0.614	0.600	0.457
	Nb	−0.0079	−0.0145	−0.164	−0.186	
	B	−0.0070	−0.0350	–	−0.042	
$Fe_{70}Nb_{10}B_{20}$	Fe	−0.0014	−0.0094	0.640	0.629	
	Nb	−0.0065	−0.0128	−0.145	−0.164	0.417
	B	−0.0063	−0.0312	–	−0.037	
$Fe_{60}Nb_{10}B_{30}$	Fe	−0.0007	−0.0081	0.681	0.672	
	Nb	−0.0050	−0.0109	−0.109	−0.125	0.380
	B	−0.0055	−0.0284	–	−0.034	

3.6. Correlation of crystallization mechanism with GFA

Based on atomic structural information obtained by *ab initio* molecular dynamical simulation, we propose a schematic map for the local atomic configuration of ternary Fe–Nb–B MGs and try to explain different crystallization modes, crystalline phases and GFA between $Fe_{80}Nb_{10}B_{10}$ and other two alloys that $Fe_{70}Nb_{10}B_{20}$, and $Fe_{60}Nb_{10}B_{30}$.

In $Fe_{80}Nb_{10}B_{10}$ MG, B atom always occupies the center of < 0 2 8 0 > polyhedron with one Nb atom in its neighborhood, as seen in Fig. 10 (a). B atoms are isolated from other B atoms. The structure of $Fe_{80}Nb_{10}B_{10}$ metallic glass can be considered as that Nb and B atoms linked in pairs are randomly distributed in Fe matrix. The Nb–B bonding will promote the formation of Fe-dominated clusters and α-Fe phase would participate in the early crystallization process, which would worsen GFA. Similar results have been obtained from studies conducted by Wang et al. [35]. The formation of α-Mn type phase is considered as the intermediate structure between < 0 3 6 4 > polyhedron and bcc atomic configuration. With increasing B content, < 0 3 6 0 > polyhedron becomes dominant in Fe–Nb–B melts. B atoms prefer to be in the center of < 0 3 6 0 > cluster and have other B atoms in its first shell, which boosts the propagation of B–B covalent bonds as indicated in Fig. 10 (a). A large number of B–B bonds in B-rich system make the local structure of the whole system more complex, which leads to a competition between different types of polyhedra.

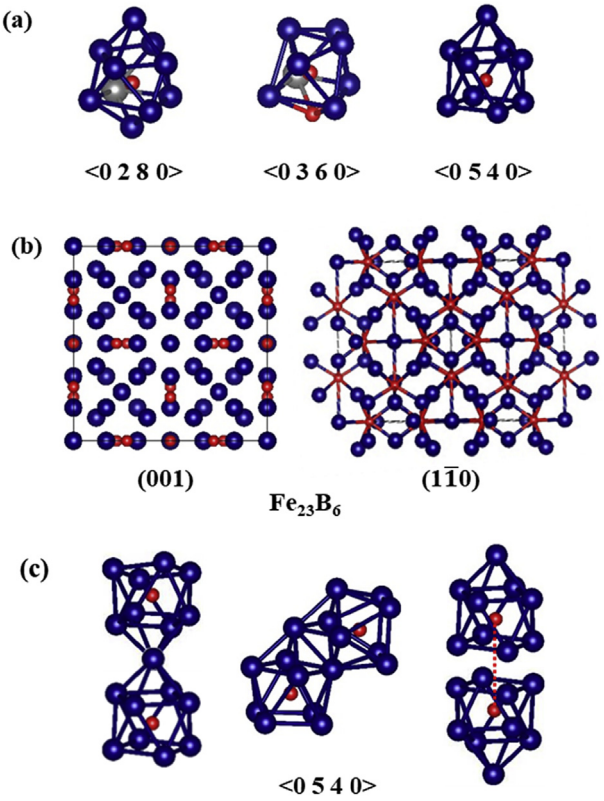

Fig. 10. (a) Polyhedra < 0 2 8 0 > , < 0 3 6 0 > centered by B atoms in the Fe–Nb–B MGs and polyhedron < 0 5 4 0 > centered by B atom in the $Fe_{23}B_6$ crystalline phase. (b) Illustration of $Fe_{23}B_6$ ($Cr_{23}C_6$-type, cF116) crystalline structure. (c) Three types of connection between two B-centered < 0 5 4 0 > clusters in the $Fe_{23}B_6$ crystalline phase. The blue, grey and red spheres stand for Fe, Nb, and B atoms, respectively.

It has been reported that a complex metastable $Fe_{23}B_6$ phase is prone to form as a primary crystallization phase in B-rich Fe–Nb–B alloys [10]. Fig. 10 (b) displays the atomic configuration of $Fe_{23}B_6$ ($Cr_{23}C_6$-type, cF116) crystalline structure. We find that only one type of polyhedron < 0 5 4 0 > polyhedron centered by B emerges in crystallized $Fe_{23}B_6$ phase, see the details in right side of Fig. 10 (a). It can be seen that this type of polyhedron has some similarities in local atomic structure as compared with B-centered < 0 2 8 0 > and < 0 3 6 0 > polyhedra. As shown in Fig.10 (a), B-centered < 0 2 8 0 > polyhedron can be seen as < 0 5 4 0 > polyhedron with one more Fe atom on its bottom site. While B-centered < 0 3 6 0 > polyhedron can be seen as < 0 5 4 0 > polyhedron losing a Fe atom on its top site and with one more B atoms on its bottom site, in the other word, B-centered < 0 5 4 0 > polyhedron turned upside down. Thus, due to the reason that the local atomic configuration of both < 0 2 8 0 > and < 0 3 6 0 > polyhedra resembles to that of < 0 5 4 0 > polyhedron, these polyhedra could transform into < 0 5 4 0 > polyhedron easily.

More interestingly, we find that there are three kinds of connection of < 0 5 4 0 > polyhedra in $Fe_{23}B_6$ crystalline phase, as seen in Fig. 10 (c). Thereby, the propagation of $Fe_{23}B_6$ crystalline structure will promote the formation of skeleton networks via the vertex, edge and face sharing of < 0 5 4 0 > polyhedra as the performance of icosahedra clusters in metal-metal-based systems such as Zr-Cu [42], which facilitates a slow dynamics [43] and a high GFA [44]. Moreover, the formation of $Fe_{23}B_6$ phase may also require abundant B–B linkages as the main skeleton just like the third type of connection shown in Fig. 10 (c). The B atom inside one of < 0 5 4 0 > polyhedron can be seen as the center of another polyhedron. Thus, the $Fe_{23}B_6$ phase only forms in the alloys with high B concentration.

On the other hand, in $Fe_{70}Nb_{10}B_{20}$ and $Fe_{60}Nb_{10}B_{30}$ MGs, the reduction of Fe-dominated clusters and the formation of < 0 3 6 0 > B-centered polyhedron as the temperature decreasing down to 300 K might inhibit the formation of Fe-centered bcc-like < 0 3 6 4 > polyhedron as shown in Fig. 4. Thus, the precipitation of α-Fe bcc-phase can be hindered. We can conclude here that the addition of B benefits the formation of the complex metastable $Fe_{23}B_6$ phase and hinders the precipitation of α-Fe phase, which are the main reasons for the improved GFA in B-rich system.

We also find that, when the content of B rises from 20% to 30%, the percentage of B-centered < 0 3 6 0 > polyhedral begins to decrease (see Figs. 5 and 6), which implies the deterioration of GFA. Meanwhile, the magnetic performance also deteriorates with metalloid-element addition. Therefore, we can choose a proper metalloid addition, e.g. 10 to 20 at.%, to achieve a high performance on both GFA and magnetism

[4].

4. Conclusions

In this work, the generalized/partial pair correlation functions, Voronoi polyhedra and CN in ternary Fe–Nb–B alloys were studied in details by using *ab initio* molecular dynamical simulations. The corresponding crystallization modes and the correlated GFA and magnetism were discussed as well.

By comparing the atomic bonding preference of $Fe_{80}Nb_{10}B_{10}$, $Fe_{70}Nb_{10}B_{20}$, and $Fe_{60}Nb_{10}B_{30}$ three alloy systems, we find that B atoms intend to be surrounded by both Nb and Fe atoms in the nearest-neighbor shell and by B atoms as the second neighbor. It leads to a small amount of direct B–B bonds in B-poor $Fe_{80}Nb_{10}B_{10}$ system. Meanwhile, the competition of Nb with Fe facilitates the precipitation of Fe-dominated α-Fe phase, which worsens the GFA of $Fe_{80}Nb_{10}B_{10}$. With the addition of B, B-centered tricapped trigonal prisms < 0 3 6 0 > Voronoi polyhedron with direct B–B bonds as a substitution of the dominant antiprisms < 0 2 8 0 > polyhedron in B-poor $Fe_{80}Nb_{10}B_{10}$ system, is more likely to propagate in B-rich $Fe_{70}Nb_{10}B_{20}$ and $Fe_{60}Nb_{10}B_{30}$ melts and glassy alloys. We also find that there is only one type of B-centered < 0 5 4 0 > polyhedron in complex $Fe_{23}B_6$ crystalline phase, which has a similar atomic configuration as that of < 0 3 6 0 > polyhedron centered by B found in $Fe_{70}Nb_{10}B_{20}$ and $Fe_{60}Nb_{10}B_{30}$. It promotes the propagation of $Fe_{23}B_6$ phase in B-rich system via abundant direct B–B linkages. The precipitation of the complex $Fe_{23}B_6$ phase instead of bcc α-Fe phase contributes to the excellent GFA of B-rich $Fe_{70}Nb_{10}B_{20}$ and $Fe_{60}Nb_{10}B_{30}$ systems. Moreover, a covalent characteristics of direct B–B bonds with a high charge density between B–B atomic pairs was confirmed here by the electronic DOS and the charge density distribution calculated with spin polarization. These bonds favor the construction of a skeleton network structure in virtue of three kinds connection of B-centered < 0 5 4 0 > polyhedron, which prevents atomic motion in $Fe_{23}B_6$ phase and further leads to a better GFA of B-rich system.

On the other hand, the negative spin polarization of both Nb and B leads to the worst magnetic performance in $Fe_{60}Nb_{10}B_{30}$, despite of the largest average magnetic moments of Fe in this ternary alloy among others. Therefore, from material design standpoint, the proper metalloid addition with the content of B between 10 and 20 at.% was chosen in Fe–Nb–B alloy systems for achieving a high performance on both GFA and magnetism. This work on the local atomic and electronic environment around metalloid B atoms in Fe–Nb–B systems may help us better understand the GFA and magnetic performance of metal-metalloid-based glassy alloys.

Acknowledgments

This work was supported by the National Natural Science Foundation of China (Grant Nos. 51601038 and 51631003), the State Key Development Program for Basic Research of China (Grant No. 2016YFB0300502), the Natural Science Foundation of Jiangsu Province, China (Grant No. BK20171354), Postdoctoral Fellow under the Hong Kong Scholar Scheme (Grant No. XJ2017048), Jiangsu Key Laboratory for Advanced Metallic Materials (Grant No. BM2007204) and the Fundamental Research Funds for the Central Universities (Grant No. 2242017K40189).

References

[1] A. Inoue, A. Takeuchi, B.L. Shen, Formation and functional properties of Fe-based bulk glassy alloys, Mater. Trans. 42 (2001) 970–978.
[2] Y. Yoshizawa, S. Oguma, K. Yamauchi, New Fe-based soft magnetic-alloys composed of ultrafine grain-structure, J. Appl. Phys. 64 (1988) 6044–6046.
[3] A. Inoue, B.L. Shen, C.T. Chang, Super-high strength of over 4000 MPa for Fe-based bulk glassy alloys in $[(Fe_{1-x},Co_x)]_{0.75}B_{0.2}Si_{0.05}]_{96}Nb_4$ system, Acta Mater. 52 (2004) 4093–4099.
[4] A. Inoue, B. Shen, Soft magnetic bulk glassy Fe-B-Si-Nb alloys with high saturation magnetization above 1.5 T, Mater. Trans. 43 (2002) 766–769.
[5] M. Stoica, K. Hajlaoui, A. Lemoulec, A.R. Yavari, New ternary Fe-based bulk metallic glass with high boron content, Phil. Mag. Lett. 86 (2006) 267–275.
[6] A. Hirata, Y. Hirotsu, T. Ohkubo, E. Matsubara, A. Makino, Local structure studies of Fe-Nb-B metallic glasses using electron diffraction, J. Microsc-OXFORD 223 (2006) 191–194.
[7] M. Imafuku, S. Sato, H. Koshiba, E. Matsubara, A. Inoue, Structural variation of Fe-Nb-B metallic glasses during crystallization process, Scripta Mater. 44 (2001) 2369–2372.
[8] X.Y. Xiong, T.R. Finlayson, B.C. Muddle, Nanocrystalline microstructures in $Fe_{93-x}Zr_7B_x$ alloys, J. Mater. Sci. 38 (2003) 1161–1169.
[9] B. Yao, L. Si, H. Tan, Y. Zhang, Y. Li, Effects of high boron content on crystallization, forming ability and magnetic properties of amorphous $Fe_{91-x}Zr_5B_xNb_4$ alloy, J. Non-Cryst. Solids 332 (2003) 43–52.
[10] M. Imafuku, S. Sato, H. Koshiba, E. Matsubara, A. Inoue, Crystallization behavior of amorphous $Fe_{90-X}Nb_{10}B$ < SUB > X < /SUB > (X = 10 and 38) alloys, Mater. Trans., JIM 41 (2000) 1526–1529.
[11] A. Hirata, Y. Hirotsu, E. Matsubara, Local atomic structures of amorphous $Fe_{80}B_{20}$ and $Fe_{70}Nb_{10}B_{20}$ alloys studied by electron diffraction, Mater. Trans. 46 (2005) 2781–2784.
[12] R.C. O'Handley, R. Hasegawa, R. Ray, C.P. Chou, Ferromagnetic properties of some new metallic glasses, Appl. Phys. Lett. 29 (1976) 330–332.
[13] R.C. O'Handley, R. Hasegawa, R. Ray, C.P. Chou, Magnetic-properties to $TM_{80}P_{20}$ glasses, J. Appl. Phys. 48 (1977) 2095–2096.
[14] B.W. Corb, R.C. O'Handley, N.J. Grant, Chemical bonding, magnetic-moments, and local symmetry in transition-metal metalloid alloys, Phys. Rev. B 27 (1983) 636–641.
[15] K. Tamura, H. Endo, Ferromagnetic properties of amorphous nickel, Phys. Lett. 29A (1969) 52–53.
[16] D.J. Sordelet, R.T. Ott, M.Z. Li, S.Y. Wang, C.Z. Wang, M.F. Besser, A.C.Y. Liu, M.J. Kramer, Structure of Zr_xPt_{100-x} ($73 \le x \le 77$) metallic glasses, Metall. Mater. Trans. A-Phys. Metall. Mater. Sci 39A (2008) 1908–1916.
[17] Q. Yu, X.D. Wang, H.B. Lou, Q.P. Cao, J.Z. Jiang, Atomic packing in Fe-based metallic glasses, Acta Mater. 102 (2016) 116–124.
[18] K. Saksl, P. Jovari, H. Franz, Q.S. Zeng, J.F. Liu, J.Z. Jiang, Atomic structure of $Al_{89}La_6Ni_5$ metallic glass, J. Phys.-Condes. Matter 18 (2006) 7579–7592.
[19] W.K. Luo, H.W. Sheng, F.M. Alamgir, J.M. Bai, J.H. He, E. Ma, Icosahedral short-range order in amorphous alloys, Phys. Rev. Lett. 92 (2004) 145502.
[20] H.W. Sheng, W.K. Luo, F.M. Alamgir, J.M. Bai, E. Ma, Atomic packing and short-to-medium-range order in metallic glasses, Nature 439 (2006) 419–425.
[21] K. Itoh, K. Hashi, K. Aoki, K. Mori, M. Sugiyama, T. Fukunaga, Atomic configuration of metal atoms in $(Ti_{0.676}Zr_{0.324})D_{0.31}$ metallic glass studied by X-ray, neutron diffraction and reverse Monte Carlo modeling, J. Alloy. Comp. 434 (2007) 180–182.
[22] G.Q. Li, K.B. Borisenko, Y.X. Chen, D. Nguyen-Manh, E. Ma, D.J.H. Cockayne, Local structure variations in $Al_{89}La_6Ni_5$ metallic glass, Acta Mater. 57 (2009) 804–811.
[23] I. Kaban, P. Jovari, A. Waske, M. Stoica, J. Bednarcik, B. Beuneu, N. Mattern, J. Eckert, Atomic structure and magnetic properties of Fe-Nb-B metallic glasses, J. Alloy. Comp. 586 (2014) S189–S193.
[24] H. Wang, T. Hu, T. Zhang, Atomic, electronic and magnetic properties of $Fe_{80}P_{11}C_9$ amorphous alloy: a first-principles study, Physica B 411 (2013) 161–165.
[25] N. Jakse, A. Pasturel, Correlation between dynamic slowing down and local icosahedral ordering in undercooled liquid $Al_{80}Ni_{20}$ alloy, J. Chem. Phys. 143 (2015) 084508.
[26] W. Zhang, Q. Li, H. Duan, Study of the effects of metalloid elements (P, C, B) on Fe-based amorphous alloys by ab initio molecular dynamics simulations, J. Appl. Phys. 117 (2015) 104901.
[27] B.S. Dong, S.X. Zhou, D.R. Li, J.Y. Qin, S.P. Pan, Y.G. Wang, Z.B. Li, Effects of solute-solute avoidance on metallic glass formation, J. Non-Cryst. Solids 358 (2012) 2749–2752.
[28] J. Ding, Y. Cheng, E. Ma, Charge-transfer-enhanced prism-type local order in amorphous $Mg_{65}Cu_{25}Y_{10}$: short-to-medium-range structural evolution underlying liquid fragility and heat capacity, Acta Mater. 61 (2013) 3130–3140.
[29] O.N. Senkov, Y.Q. Cheng, D.B. Miracle, E.R. Barney, A.C. Hannon, C.F. Woodward, Atomic structure of $Ca_{40+X}Mg_{25}Cu_{35-X}$ metallic glasses, J. Appl. Phys. 111 (2012) 123515.
[30] P.F. Guan, T. Fujita, A. Hirata, Y.H. Liu, M.W. Chen, Structural origins of the excellent glass forming ability of $Pd_{40}Ni_{40}P_{20}$, Phys. Rev. Lett. 108 (2012) 175501.
[31] G. Kresse, J. Furthmüller, Efficiency of ab-initio total energy calculations for metals and semiconductors using a plane-wave basis set, Comput. Mater. Sci. 6 (1996) 15–50.
[32] Y.Q. Cheng, E. Ma, Atomic-level structure and structure-property relationship in metallic glasses, Prog. Mater. Sci. 56 (2011) 379–473.
[33] Y. Hirotsu, T. Hanada, T. Ohkubo, A. Makino, Y. Yoshizawa, T.G. Nieh, Nanoscale phase separation in metallic glasses studied by advanced electron microscopy techniques, Intermetallics 12 (2004) 1081–1088.
[34] T. Fukunaga, et al., Voronoi analysis of the structure of Cu-Zr and Ni-Zr metallic glasses, Intermetallics 14 (2006) 893–897.
[35] Y. Wang, Y. Zhang, A. Takeuchi, A. Makino, Y. Kawazoe, Investigation on the crystallization mechanism difference between FINEMET (R) and NANOMET (R) type Fe-based soft magnetic amorphous alloys, J. Appl. Phys. 120 (2016) 145102.
[36] D. Mayou, D. Nguyen-Manh, A. Pasturel, F. Cyrot-Lackmann, Model for the hybridization effect in disordered-systems, Phys. Rev. B 33 (1986) 3384–3391.
[37] N.F. Mott, Electrons in transition metals, Adv. Phys. 13 (1964) 325–413.
[38] Y.B. Xu, D. Greig, A.L. Mitchell, E.A. Seddon, J.A.D. Matthew, The spin-dependent electronic structure of amorphous magnetic alloys, J. Appl. Phys. 81 (1997)

4419–4421.
[39] P. Ganesh, M. Widom, Ab initio simulations of geometrical frustration in supercooled liquid Fe and Fe-based metallic glass, Phys. Rev. B 77 (2008) 014205.
[40] A.P. Malozemoff, A.R. Williams, V.L. Moruzzi, Band-gap theory of strong ferromagnetism - application to concentrated crystalline and amorphous Fe-metalloid and Co-metalloid alloys, Phys. Rev. B 29 (1984) 1620–1632.
[41] H. Tian, C. Zhang, J.J. Zhao, C. Dong, B. Wen, Q. Wang, First-principle study of the structural, electronic, and magnetic properties of amorphous Fe-B alloys, Physica B 407 (2012) 250–257.
[42] Y.Q. Cheng, E. Ma, H.W. Sheng, Atomic level structure in multicomponent bulk metallic glass, Phys. Rev. Lett. 102 (2009) 245501.
[43] Y.C. Hu, F.X. Li, M.Z. Li, H.Y. Bai, W.H. Wang, Five-fold symmetry as indicator of dynamic arrest in metallic glass-forming liquids, Nat. Commun. 6 (2015) 8310.
[44] M. Li, C.Z. Wang, S.G. Hao, M.J. Kramer, K.M. Ho, Structural heterogeneity and medium-range order in Zr_xCu_{100-x} metallic glasses, Phys. Rev. B 80 (2009) 184201.